

## Article

# Solidification Mechanism of Microstructure of Al-Si-Cu-Ni Alloy Manufactured by Laser Powder Bed Fusion and Mechanical Properties Effect

Zhichao Shi <sup>1</sup> , Pengfei Yan <sup>2</sup> and Biao Yan <sup>1,3,\*</sup>

<sup>1</sup> School of Materials Science and Engineering, Tongji University, Shanghai 201804, China; 2132881@tongji.edu.cn

<sup>2</sup> Eighth Research Institute of Nuclear Industry, Shanghai 201800, China; yanpengfei@cnnmail.cn

<sup>3</sup> Shanghai Key Laboratory for R&D and Application of Metallic Functional Materials, Shanghai 201804, China

\* Correspondence: 84016@tongji.edu.cn; Tel.: +86-133-1193-7802

**Abstract:** Based on previous work, where Al-Si-Cu-Ni alloy was successfully manufactured by laser powder bed fusion (PBF-LB/M) technology, in this study, we further observe the microstructure of the alloy, analyze the formation mechanism of the microstructure during solidification, and discuss their implications for the mechanical properties. The results indicate that the microstructure comprises multi-level cellular heterogeneous structures, with an  $\alpha$ -Al matrix in the interior of the cellular structure and Cu- and Ni-rich phases clustered at the boundaries, intertwined with the silicon network. During solidification,  $\alpha$ -Al solidifies first and occupies the core of the cells, while Si phases and Cu- and Ni-rich phases deposit along the cellular boundaries under the influence of surface tension. During the solidification process of cellular boundaries, influenced by spinodal decomposition and lattice spacing, Si phases and Cu- and Ni-rich phases interconnect and distribute crosswise, collectively forming multi-level cellular structures. The refined cellular microstructure of the PBF-LB/M Al-Si-Cu-Ni alloy enhances the mechanical properties of the alloy. The alloy exhibits a bending strength of  $766 \pm 30$  MPa, a tensile strength and yield strength of  $437 \pm 6$  MPa and  $344 \pm 4$  MPa, respectively, with a relatively low fracture elongation of approximately  $1.51 \pm 0.07\%$ . Subsequent improvement can be achieved through appropriate heat treatment processes.

**Keywords:** laser powder bed fusion; al-si alloy; microstructure; solidification mechanism; mechanical properties



**Citation:** Shi, Z.; Yan, P.; Yan, B.

Solidification Mechanism of Microstructure of Al-Si-Cu-Ni Alloy Manufactured by Laser Powder Bed Fusion and Mechanical Properties Effect. *Metals* **2024**, *14*, 586. <https://doi.org/10.3390/met14050586>

Academic Editors: Pavel Krakhmalev and Thomas Niendorf

Received: 2 April 2024

Revised: 9 May 2024

Accepted: 15 May 2024

Published: 17 May 2024



**Copyright:** © 2024 by the authors. Licensee MDPI, Basel, Switzerland. This article is an open access article distributed under the terms and conditions of the Creative Commons Attribution (CC BY) license (<https://creativecommons.org/licenses/by/4.0/>).

## 1. Introduction

Laser Powder Bed Fusion (PBF-LB/M) technology is an additive manufacturing technique for direct and rapid fabrication of metal components. During the PBF-LB/M process, the cooling rate is exceptionally high, reaching up to  $10^6$ – $10^8$  °C/s [1], resulting in a fine-grained and dense alloy microstructure with uniform elemental distribution, thereby enhancing the mechanical properties of the alloy. Al-Si alloys are lightweight materials renowned for their excellent castability and mechanical properties [2–4]. With the advancement of high-end manufacturing and the pursuit of rapid prototyping, Al-Si alloy materials have demonstrated remarkable performances in laser powder bed fusion technology [5]. Mei et al. [6] achieved extremely fine microstructures and excellent mechanical properties in an AlSi<sub>10</sub>Mg alloy manufactured via PBF-LB/M technology. Prashanth et al. [7] observed a refined eutectic silicon cellular structure in PBF-LB/M Al-12Si, which significantly increased the material's yield strength and tensile strength, respectively, four times and twice as high as conventional cast materials. The solidification mechanism of PBF-LB/M Al-Si alloys exhibits a honeycomb dendritic structure, also referred to by some scholars as a cellular heterogeneous structure. This unique alternating coarse–fine cellular heterogeneous structure has been identified as one of the key factors influencing material

mechanical properties [8]. However, most studies have primarily focused on the impact of cellular heterogeneous structures on mechanical properties, with scant reports on the formation process of cellular structures during PBF-LB/M solidification. Consequently, the mechanism underlying the formation of cellular structures during the PBF-LB/M process remains unclear.

Copper and nickel elements are important alloying elements in the aluminum alloy system [9–12], capable of forming various intermediate phases with the matrix, such as  $\text{Al}_2\text{Cu}$ ,  $\text{Al}_7\text{Cu}_4\text{Ni}$ ,  $\text{Al}_3\text{CuNi}$ ,  $\text{Al}_3\text{Ni}$ ,  $\text{Al}_3\text{Ni}_2$ , etc. Similar to the eutectic silicon network, under certain conditions they may also form a cellular heterogeneous network structure on the matrix, thereby enhancing its mechanical properties [13]. Zheng et al. [14] conducted a study on the microstructure and tensile properties of Al-Si-Cu-Mg alloys with different Cu contents and Cu/Mg ratios. The results showed the formation of  $\text{Mg}_2\text{Si}$ ,  $\theta\text{-Al}_2\text{Cu}$ , and Q-type intermetallic phases in the as-cast Al-Si-Cu-Mg alloy. After aging treatment, a small amount of native intermetallic particles and a large amount of Q' phase appeared, resulting in high strength and good ductility of the material. Rometsch et al. [15] reported the mixing of pure nickel powder into PBF-LB/M  $\text{AlSi}_{10}\text{Mg}$  powder to achieve a composition close to the eutectic point. The study found that most submicron  $\text{Al}_3\text{Ni}$  particles obtained through in situ reactions were uniformly distributed in the matrix. The properties of parts manufactured by PBF-LB/M were significantly improved due to Orowan strengthening or the stacking fault mechanism. Nickel typically interacts with copper and aluminum, forming stable ternary phases or, under appropriate heat treatment regimes, enhancing the material's overall performance. Research by Medrano-Prieto [16] indicated that adding 2 wt% Ni to A319 aluminum alloy directly influenced the microstructure. Through the formation of Al-Fe-Ni, Al-Cu-Ni, and Al-Ni intermetallic compounds, the hardness after aging treatment was significantly higher than that of the original sample.

In previous work, we successfully manufactured the Al-Si-Cu-Ni alloys using laser powder bed fusion technology [17]; however, the microstructure, solidification mechanism, and influence on the mechanical properties of the alloys are unclear. In this work, we thoroughly study the microstructure and formation mechanism of PBF-LB/M Al-Si-Cu-Ni alloys and discuss their effects on mechanical properties.

## 2. Materials and Methods

In previous work [17], a PBF-LB/M Al-Si-Cu-Ni alloy has been manufactured by using optimal process parameters (laser powder—290 W, scanning speed—1000 mm/s, layer thickness—30  $\mu\text{m}$ , hatch distance—40  $\mu\text{m}$ , scanning strategy—stripes) (specific compositions of the alloy powders used are shown in Table 1 and will not be described here).

**Table 1.** The nominal composition of each element of the mixed alloy powder [17].

Element	Al	Si	Cu	Ni	Fe	Re
Element Weight (wt%)	Bal.	12.0	3.8	2.0	0.2	0.05

After separating the samples and substrates using a wire-cutting machine, they undergo a 1 h ultrasonic cleaning process to thoroughly remove surface oil and other contaminants. Subsequently, each sample is subjected to SiC sandpaper grinding and polishing. Following this, an etching process is performed using Keller's reagent (2.5 mL  $\text{HNO}_3$  + 1.5 mL  $\text{HCl}$  + 1.5 mL  $\text{HF}$  + 95 mL  $\text{H}_2\text{O}$ ) with an etching time of approximately 15 s. The microstructure of the samples is observed using a scanning electron microscope (SEM, Zeiss Gemini 300, Oberkochen, Germany). X-ray diffraction (XRD, Bruker, D8 Advance, Karlsruhe, Germany) analysis is conducted using  $\text{Cu K}\alpha 1$  radiation ( $\lambda = 0.15406$  nm) with a scanning range of 20–80° and a scanning speed of 1°/min, and the samples are analyzed for various properties. Microstructure, elemental distribution, phase composition, and structure analyses are performed using FIB-TEM (FEI Talos F200X G2, Waltham, MA, USA). Tensile testing is carried out using the CHT4305 universal testing machine produced by the

MTS Corporation (Eden Prairie, MI, USA), employing axial tension with a testing rate of 0.5 mm/min. Three different samples were tested, and their average values were taken as the final tensile performance.

### 3. Results and Discussion

#### 3.1. Phases of Powder and Samples

Figure 1 illustrates the X-ray diffraction (XRD) patterns of the Al-Si-Cu-Ni alloy powder and the as-built sample. As depicted in Figure 1, beyond the diffraction peaks of Al and Si, there are also minor peaks corresponding to binary phases of Al-Cu and Al-Ni, as well as ternary phases of Al-Cu-Ni. This observation is consistent with reported phases in the literature [18–20]. Notably, no peaks corresponding to elemental Cu or Ni are detected, indicating that sufficient alloying of Cu and Ni elements has occurred after PBF-LB/M processing. A leftward shift of the diffraction peaks of  $\alpha$ -Al is observed in the as-built sample compared to the alloy powder, suggesting lattice distortion within the samples. In the Al-Si system, substitutional solid solutions are commonly formed. Since the atomic radii of Cu and Ni are significantly larger than that of Al, the incorporation of Cu and Ni atoms into the  $\alpha$ -Al lattice leads to an increase in lattice constants and interplanar spacings, resulting in a leftward shift of the diffraction peaks, consistent with the XRD diffraction patterns.

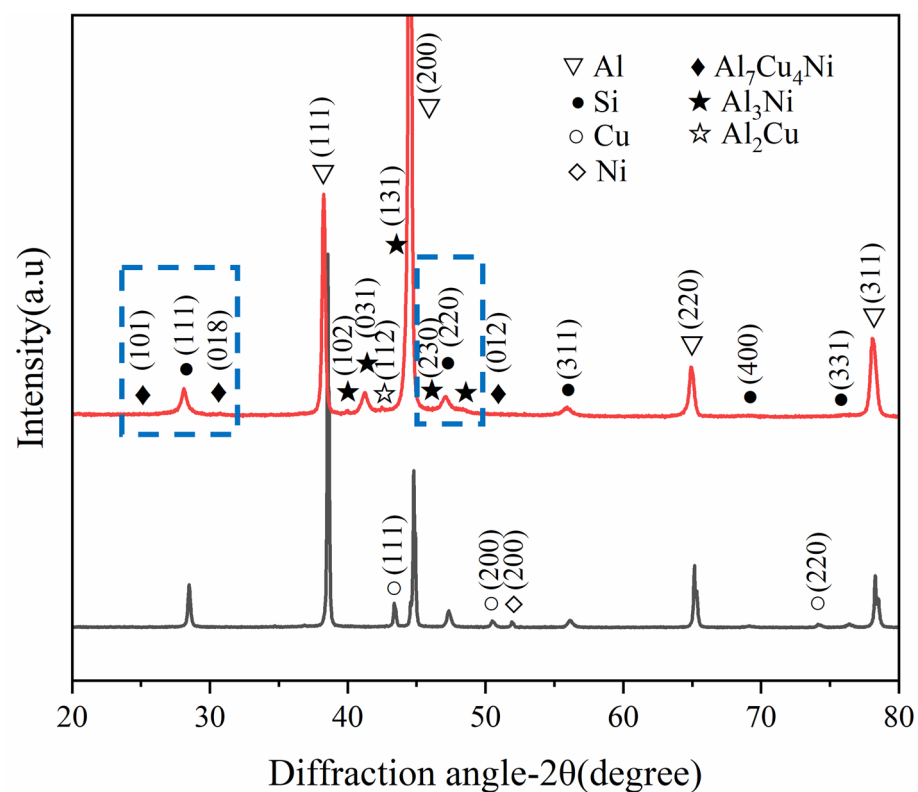


**Figure 1.** XRD of powder and as-built sample of Al-Si-Cu-Ni.

#### 3.2. Microstructure of PBF-LB/M Al-Si-Cu-Ni Alloys

Figure 2a,b depict the microstructure of the top surface of the PBF-LB/M Al-Si-Cu-Ni alloy at low and high magnifications, with Figure 2b providing an enlarged view within the yellow dashed box in Figure 2a. At low magnification, the morphology of the melt pool and its boundaries are clearly visible. At high magnification, the microstructure is revealed to be composed of a fine  $\alpha$ -Al matrix with cellular structures distributed on it. This is consistent with descriptions found in most of the literature [21–23]. However, in contrast to most of the literature that mentions eutectic silicon networks, in this study, these are second phases formed by Cu and Ni element-enriched regions. They are uniformly distributed around

the silicon network, forming a multi-layered cellular heterogeneous microstructure with alternating distributions. The melt pool region is divided into coarse and fine zones. The formation of coarse zones and fine zones is related to the laser scanning method. Coarse zones are primarily formed due to repeated laser scanning or, in other words, the stacking of melt pools, which is related to process parameters such as the scanning spacing. A smaller scanning spacing results in a larger stacking range between adjacent melt pools, leading to a larger remelting area and a higher proportion of coarse zones. Additionally, if the input laser energy is higher, more heat is radiated in that area, providing sufficient driving force for the continued growth of cellular structures. The formation of fine zones is related to heterogeneous nucleation. As the laser scans across the powder layer to form a metal melt, it remelts the previously solidified metal thin layer. Due to the excellent absorption and heat dissipation of solidified metal, the re-melted thin layer generates a significant undercooling, forming many initial nuclei. The proximity of these nuclei hinders each other's growth, resulting in a substantial reduction in the size of substructure cells within the grains, ultimately forming fine zones.

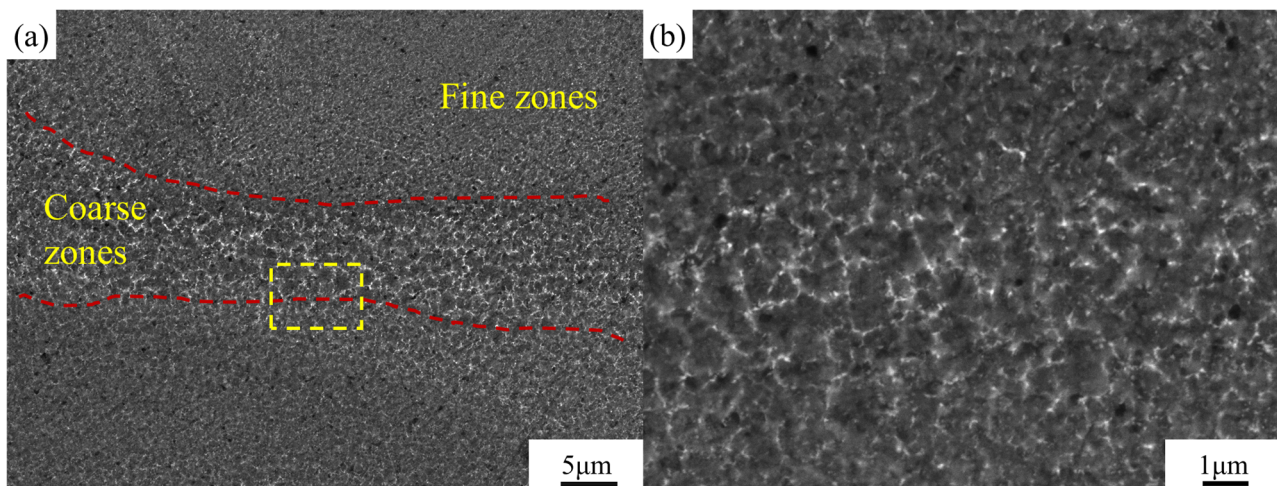


**Figure 2.** The microstructure of Al-Si-Cu-Ni samples: (a) low magnification; (b) enlarged view of the yellow box in (a).

To gain a clearer understanding of the microstructure and phase composition of the top surface of Al-Si-Cu-Ni alloy samples, FIB-TEM analysis is conducted, and the results are presented in Figures 3 and 4. Figure 3a,b display the macroscopic features of the sample under bright-field and dark-field environments, with different contrast regions revealing distinct phase compositions. Similar to Figure 2, at a smaller scale, the morphological features of the cellular structures become more pronounced. These cellular structures are microscopic substructures distributed on micron-sized grains, with a scale of around a few hundred nanometers. The formation of such structures is attributed to the rapid cooling rate and small component undercooling during the PBF-LB/M process, along with the unique laser scanning method [24]. Figure 3c,d showcase finer details of the cellular structure region and present EDS mapping results. It can be observed that the grains of the Al-Si-Cu-Ni alloy consist of cellular structures with sizes ranging from 200 to 500 nm, and the cellular boundaries are enriched with Cu, Ni, and Si elements. Notably, the silicon network intertwines with the Cu- and Ni-rich network, collectively forming smaller-sized multi-level cellular heterogeneous structures. These structures are significantly smaller than the cellular structure size of traditional Al-Si alloy (approximately 500 nm). This feature is expected to have a positive impact on the mechanical properties of the alloy.

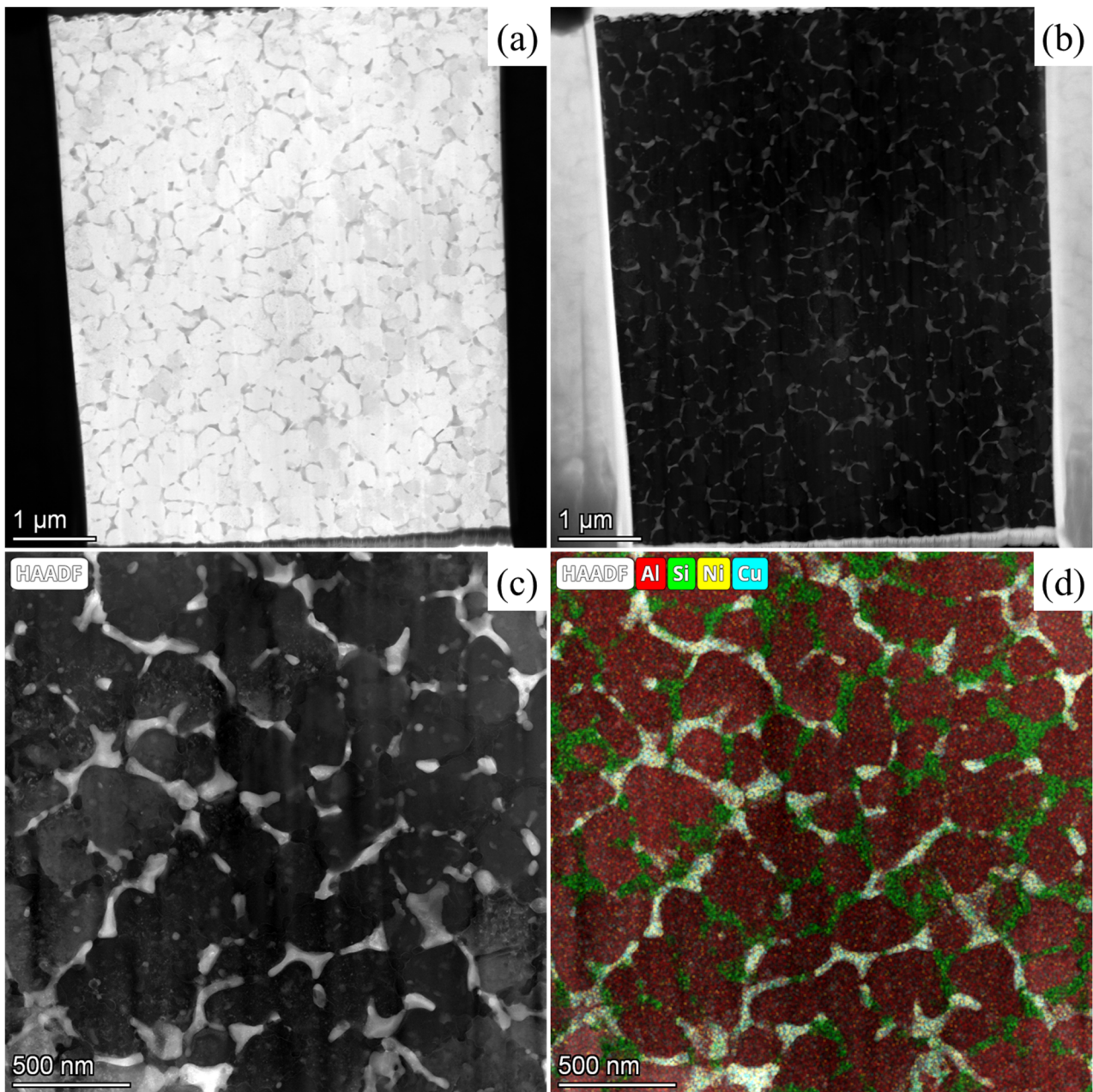


**Figure 3.** TEM images of microstructural characteristics on the top surface of PBF-LB/M Al-Si-Cu-Ni samples: (a) bright-field image; (b) dark-field image; (c) HAADF morphology; (d) EDS mapping element distribution.

Figure 4 illustrates the distribution of nanoscale particles and the structure of precipitated phases in the Al-Si-Cu-Ni alloy. Due to the different contrasts in phases, it is easy to distinguish the Si phase (blue arrows) and the Cu-rich and Ni-rich phases (red arrows). The Cu-rich and Ni-rich phases exhibit rod-like or herringbone distribution, forming a cellular network structure along with the Si phase, featuring the  $\alpha$ -Al matrix at its core. Figure 4b–e present HRTEM images and corresponding FFT results of the Cu, Ni-enriched regions, further confirming the phase composition and structure of the PBF-LB/M Al-Si-Cu-Ni alloy. In these regions, the presence of  $\text{Al}_7\text{Cu}_4\text{Ni}$  and  $\text{Al}_3\text{Ni}$  phases is consistent with the XRD results (Figure 1). During the deformation processes, these nanoscale precipitates will hinder the movement of dislocations through the Orowan mechanism, contributing to the further improvement of the mechanical properties of the Al-Si-Cu-Ni alloy.

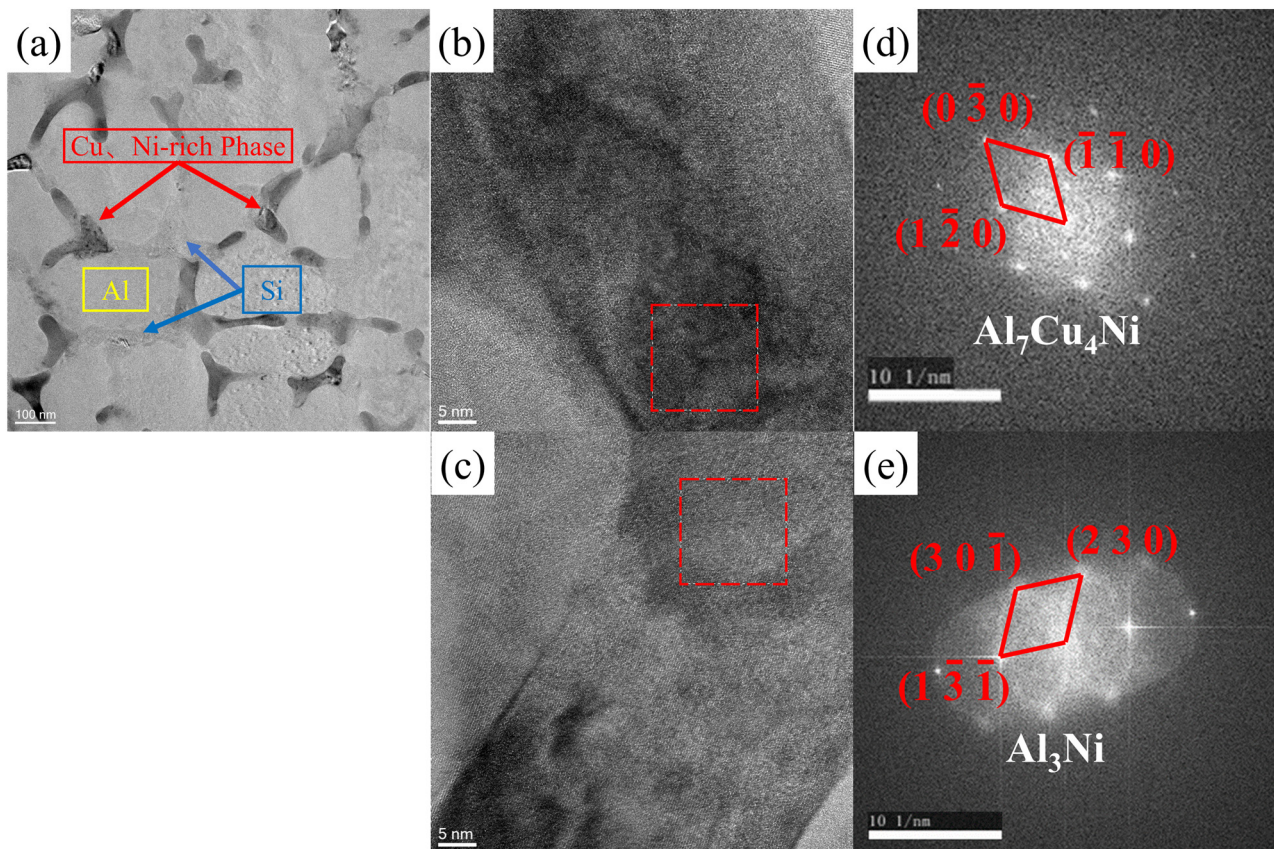


**Figure 4.** TEM images of PBF-LB/M Al-Si-Cu-Ni samples: (a) bright-field image of  $\alpha$ -matrix and cellular structure; (b–e) HRTEM images of  $\text{Al}_7\text{Cu}_4\text{Ni}$ ,  $\text{Al}_3\text{Ni}$ , and FFT results of the corresponding regions.

### 3.3. Solidification Mechanism of PBF-LB/M Al-Si-Cu-Ni Alloys

The Al-Si-Cu-Ni alloy manufactured by laser powder bed fusion exhibits a typical honeycomb-cellular heterogeneous microstructure, with the cellular structures enriched at the edges with Cu, Ni phases, and silicon phases. It is generally believed that the formation of cellular structures requires the existence of a minimal degree of undercooling, where the solute concentration in the liquid phase must be extremely low and coordinated with an extremely high solidification rate at the solid–liquid interface [7]. Taking  $\text{AlSi}_{12}$  as an example, during the solidification process of  $\text{AlSi}_{12}$ , the solid–liquid interface pushes the Si elements into the liquid. Therefore, as the solid–liquid interface moves, the solute concentration in the liquid increases. Additionally, it can be observed from the Al-Si phase diagram that the solubility of Si in Al decreases with temperature. At the eutectic temperature (850 K), the solubility of Si in Al is 1.65 wt%, decreasing to 0.06 wt% at 573 K. Under the extremely high cooling rate of PBF-LB/M, a large number of Si atoms are retained in the  $\alpha$ -Al matrix in an oversaturated state, leading to a significant reduction in the concentration of Si in the liquid phase at the solid–liquid interface. This, in turn, reduces the solute concentration and undercooling. In this scenario, the formation of cellular structure is given priority.

In the laser powder bed fusion process, some process features are not visible in conventional solidification processes. Therefore, in addition to the above-mentioned constitutional supercooling theory and interfacial stability theory, other physical factors need to be considered. Similar phenomena have been observed in other alloy systems [7,25–27]. During the solidification process, and under the influence of kinetic conditions, the low-melting phase ( $\alpha$ -Al phase) is solidified first by rejecting high-melting solutes (such as Si phases, Cu- and Ni-rich phases) at the forefront of the solid–liquid interface. The low-melting phase occupies the core of the cellular structure. Due to the high laser-scanning speed and

temperature generated during the PBF-LB/M forming process (far exceeding the melting point), the melt pool experiences a very high temperature gradient, resulting in intense Marangoni convection [28,29]. This temperature gradient generates surface tension gradients, causing high-melting phases (such as Si phase, Cu- and Ni-rich phases) to flow from areas with lower surface tension to areas with higher surface tension. They deposit along the boundaries of the cellular structure through a particle-accumulated structure-formation mechanism (PAS mechanism) [30].

Regarding the phenomenon of Si, and Cu- and Ni-phases' complementary interweaving in the cellular network structure, we speculate that this may be due to spinodal decomposition occurring during the solidification process at cellular boundaries, possibly related to the enrichment of Cu and Ni solutes. According to non-equilibrium solidification theory [31–34], any chemical fluctuations can lead to “uphill diffusion” and “spinodal decomposition” [31,35]. This phenomenon has been confirmed in high-entropy alloys due to the “slow diffusion” of solutes [35,36]. Because the high cooling rate generated in the PBF-LB/M process leads to “insufficient diffusion”, spinodal decomposition may occur. Chemical fluctuations caused by solute segregation lead to spinodal decomposition during cellular boundary solidification, consistent with the findings of Li et al. regarding the laser additive manufacturing of (LAM) 316L stainless steel [37]. Due to spinodal decomposition, the Si phases and Cu- and Ni-rich phases are interconnected, with a transitional region, which is consistent with the case of Si connecting with Cu- and Ni-rich phases shown in Figure 3. A schematic diagram of spinodal decomposition is shown in Figure 5d.

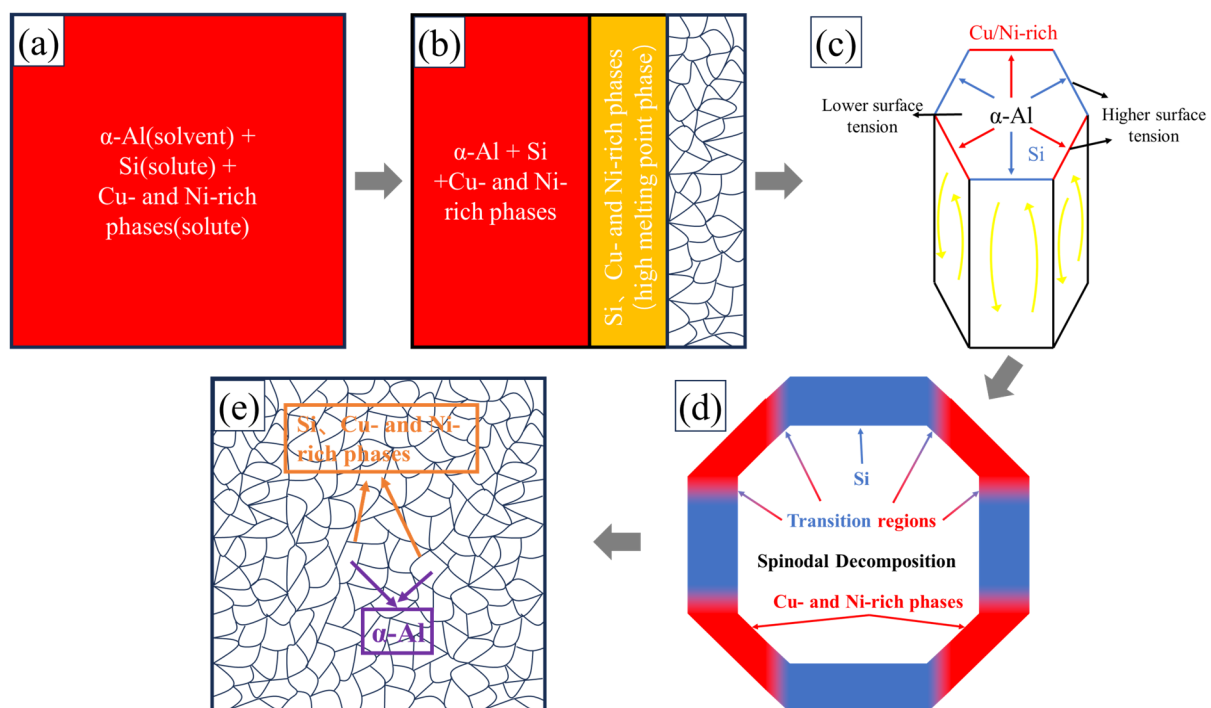


**Figure 5.** Schematic diagram of the formation of the cellular structure of PBF-LB/M Al-Si-Cu-Ni: (a) melt, (b–c) flow of high melting point phases, (d) spinodal decomposition and (e) cellular structure.

The cross-distribution between the Si and the Cu- and Ni-rich phases may be related to the interplanar spacing. Figure 6 illustrates the  $\text{Al}_7\text{Cu}_4\text{Ni}$  and  $\text{Al}_3\text{Ni}$  phases along with their FFT and IFFT images. From Figure 6d,e, it can be observed that the  $\text{Al}_7\text{Cu}_4\text{Ni}$  phases primarily have (015) and (107) crystal planes, with the interplanar spacings being measured through IFFT transformations as  $d(015) = 0.323$  nm and  $d(107) = 0.312$  nm, as shown in Figure 6g,h. The theoretical interplanar spacing of the Si(111) crystal plane is 0.314 nm, which is close to the interplanar spacings of the  $\text{Al}_7\text{Cu}_4\text{Ni}$  phase's (015) and (107) crystal planes. Additionally, the interplanar spacing of the  $\text{Al}_3\text{Ni}$  phase's (212) crystal plane is

$d(212) = 0.20$  nm, close to the interplanar spacing of the Si(220) crystal plane (0.192 nm). Due to the similar interplanar spacings, during the process of spinodal decomposition, there might be a certain orientation relationship between the Si phase and the Cu- and Ni-rich phases, leading to their cross-distribution state. The XRD also shows that the peaks of the  $\text{Al}_7\text{Cu}_4\text{Ni}$  phases and some  $\text{Al}_3\text{Ni}$  phases are very close to the peaks of Si(111) and Si(220) (as indicated by the blue dashed box in Figure 1), further supporting this conclusion. Therefore, during the solidification process at cellular boundaries, spinodal decomposition results in the interconnected state between the Si and the Cu- and Ni-rich phases. Due to the close interplanar spacings, there may be a certain orientation relationship between them, resulting in the cross-distribution state between the Si and the Cu- and Ni-rich phases. These two reasons together contribute to the formation of complementary interwoven cellular microstructure features between the Si and the Cu- and Ni-rich phases.

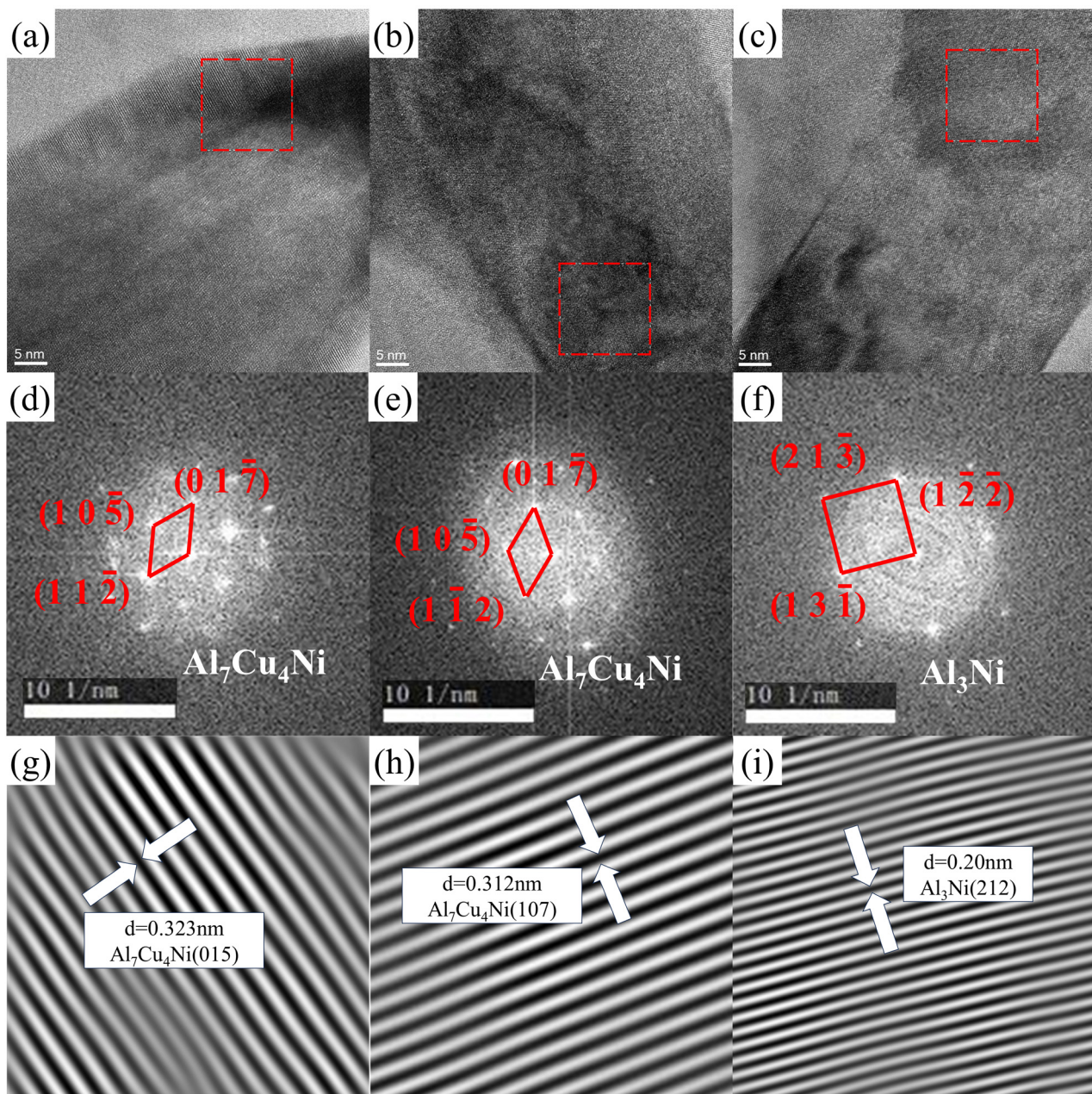


Figure 6. (a–c) HRTEM images, (d–f) FFT results, and (g–i) IFFT results.

In summary, the solidification process of the PBF-LB/M Al-Si-Cu-Ni alloy can be described as follows (as shown in Figure 5): During the PBF-LB/M process, due to the extremely high cooling rate,  $\alpha$ -Al undergoes primary solidification, and a large amount of Si is retained within the  $\alpha$ -Al matrix, increasing the solubility of Si in Al. The  $\alpha$ -Al occupies the core of the cellular structure, while the Si and the Cu- and Ni-rich phases are rejected from the Al matrix into the melt. Under the influence of surface tension, they diffuse along the boundaries of the cellular structure, accumulating and ultimately solidifying at the cellular boundaries. During the solidification at cellular boundaries, the high cooling rate leads to insufficient solute diffusion, resulting in solute segregation and spinodal decomposition. Some crystal plane spacings between the Si and the Cu- and Ni-rich phases are similar, facilitating the interconnection and cross-distribution between the Si and Cu- and Ni-rich phases, forming a complementary interwoven structure. Therefore, within the Al-Si-Cu-Ni alloy, a multi-level heterogeneous microstructure is formed, featuring a network of Cu- and Ni-rich cells complementarily interwoven with a silicon network.

### 3.4. Mechanical Properties of PBF-LB/M Al-Si-Cu-Ni Alloys

The above discussion reveals that, due to laser powder bed fusion being a rapid melting and solidification material-forming technology, it results in microstructures significantly different from traditional manufacturing processes. The cellular heterostructure formed in the Al-Si-Cu-Ni alloy markedly enhances the material's mechanical properties.

#### 3.4.1. Bending Property

According to our previous research [17], the Al-Si-Cu-Ni alloy manufactured by laser powder bed fusion demonstrates an outstanding bending performance. Experimental results indicate that the average bending strength of this alloy is  $766 \pm 30$  MPa, with an average fracture displacement of  $0.84 \pm 0.03$  mm. These values are significantly higher than those of aluminum alloys prepared by conventional methods [38,39], and they also surpass the reported PBF-LB/M aluminum alloys [40] and the base alloy AlSi20 ( $644 \pm 44$  MPa) [41]. This suggests that the cellular heterostructure formed in the PBF-LB/M Al-Si-Cu-Ni alloy plays a positive role in enhancing its bending property.

#### 3.4.2. Tensile Property

According to the information shown in Figure 7, the PBF-LB/M Al-Si-Cu-Ni alloy exhibits an excellent tensile performance at room temperature. The tensile strength is  $437 \pm 6$  MPa, surpassing that of horizontally cast alloys. Since aluminum alloys do not typically show a distinct yield plateau during the tensile process, the nominal yield strength of the material is often represented by the stress at 0.2% plastic strain, denoted as  $R_{0.2}$ . Therefore, the nominal yield strength of the PBF-LB/M Al-Si-Cu-Ni alloy is  $344 \pm 4$  MPa. Table 2 presents a comparison of the tensile performance between common PBF-LB/M-formed alloys and cast Al-Si alloys. It can be observed that the tensile performance of the Al-Si-Cu-Ni alloy manufactured by PBF-LB/M is superior to the PBF-LB/M AlSi12 alloy, attributed to the addition of Cu and Ni elements. Compared to the PBF-LB/M AlSi<sub>10</sub>Mg alloy, there is a slight increase in strength, and it significantly exceeds horizontally cast alloys. However, the fracture elongation of PBF-LB/M Al-Si-Cu-Ni alloy is relatively low, at approximately  $1.51 \pm 0.07\%$ . This drawback can be addressed through subsequent heat treatment processes to improve microstructure morphology and further optimize mechanical properties.

The mechanical performance of a material primarily depends on its microstructure. In the as-cast eutectic Al-Si alloys, the structures are mainly composed of coarse, elongated, or rod-shaped eutectic silicon and Al-matrices. These coarse structures tend to become stress concentration points under load, leading to premature failure and, consequently, relatively poor mechanical properties. However, in this study, the Al-Si-Cu-Ni alloy manufactured using PBF-LB/M technology exhibits a fine microstructure with a multi-level cellular het-

erostructure. Silicon phases are uniformly distributed on the Al matrix in a cellular network structure, significantly improving the material's mechanical properties. The addition of Cu and Ni elements forms a cellular heterostructure that interlaces complementarily with the silicon network, further strengthening the matrix and significantly enhancing the mechanical properties. Due to the unique characteristics of the PBF-LB/M forming process, which has a very high cooling rate, a large amount of alloying elements dissolve in the  $\alpha$ -Al matrix, forming oversaturated solid solutions. This leads to an increase in lattice distortion and strengthening effects due to the enhanced solid solution hardening. Additionally, PBF-LB/M Al-Si-Cu-Ni alloy typically contains high-density dislocations, precipitates rich in Cu and Ni, as well as cellular structures at the submicron scale and in micron-sized grains. The heterogeneity and hierarchy of this microstructure introduce numerous obstacles to the dislocation motion, increasing the material's strength. The grains in the PBF-LB/M Al-Si-Cu-Ni alloy are significantly refined, leading to a substantial reduction in grain size. According to the Hall–Petch equation [50], smaller grain sizes result in higher material strength. This is one of the reasons why the strength of the PBF-LB/M Al-Si-Cu-Ni alloy exceeds that of horizontally cast alloys produced by traditional methods.

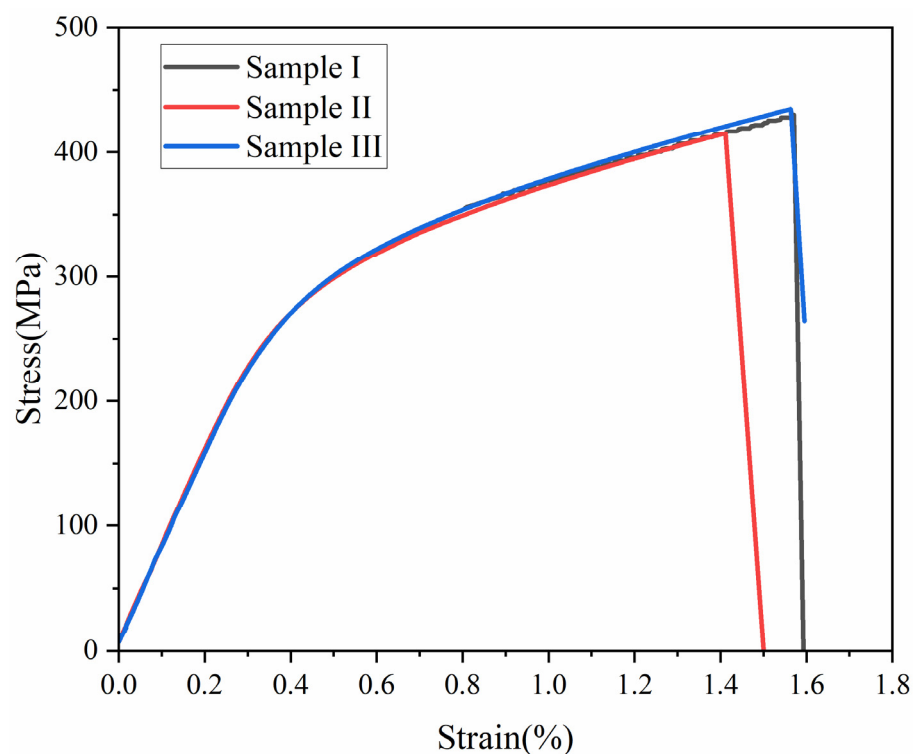


**Figure 7.** Tensile property of PBF-LB/M Al-Si-Cu-Ni alloy.

**Table 2.** Tensile strength of PBF-LB/M and cast Al-Si alloys.

Materials	PBF-LB/M (MPa)	Cast (MPa)
AlSi <sub>12</sub>	325 [42]	~
	380 [43]	~
	316 [44]	235 [45]
AlSi <sub>10</sub> Mg	357 [46]	315 [47]
	430–450 [48,49]	~

#### 4. Conclusions

Based on the previous work, we have deeply investigated three aspects of the microstructure, solidification mechanism, and its influence on the mechanical properties of PBF-LB/M Al-Si-Cu-Ni alloys. The following conclusions are drawn:

- (1) The PBF-LB/M Al-Si-Cu-Ni alloy comprises  $\alpha$ -Al, Si, and small amounts of  $\text{Al}_7\text{Cu}_4\text{Ni}$ ,  $\text{Al}_3\text{Ni}$ , and  $\text{Al}_2\text{Cu}$  phases. The complementary interlacing between the Si and the Cu- and Ni-rich phases together constitutes a cellular heterogeneous microstructure, which can significantly improve the mechanical properties of the alloy. The bending strength, fracture displacement, ultimate tensile strength, and yield strength of the alloy are  $766 \pm 30$  MPa,  $0.84 \pm 0.03$  mm,  $437 \pm 6$  MPa, and  $344 \pm 4$  MPa, but the fracture elongation is relatively low, at only  $\sim 1.51 \pm 0.07\%$ .
- (2) During the solidification process of the PBF-LB/M Al-Si-Cu-Ni alloy,  $\alpha$ -Al solidifies initially, occupying the core of the cellular structure. The high-melting-point Si and Cu- and Ni-rich phases are deposited along the boundary of the cellular structure under the influence of surface tension and undergo spinodal decomposition. Influenced by the lattice spacing, they interconnect and cross-distribute among each other, collectively forming the cellular heterogeneous microstructure.

**Author Contributions:** Conceptualization, B.Y., P.Y. and Z.S.; methodology, Z.S. and P.Y.; software, Z.S.; validation, Z.S. and P.Y.; formal analysis, Z.S.; investigation, Z.S.; resources, B.Y. and P.Y.; data curation, Z.S.; writing—original draft preparation, Z.S.; writing—review and editing, Z.S., P.Y. and B.Y.; visualization, Z.S.; supervision, P.Y.; project administration, P.Y., Z.S. and B.Y.; funding acquisition, B.Y. All authors have read and agreed to the published version of the manuscript.

**Funding:** This research received no external funding.

**Data Availability Statement:** The original contributions presented in the study are included in the article, further inquiries can be directed to the corresponding author.

**Conflicts of Interest:** Author Pengfei Yan was employed by the company Eighth Research Institute of Nuclear Industry. The remaining authors declare that the research was conducted in the absence of any commercial or financial relationships that could be construed as a potential conflict of interest.

## References

1. Mei, J.; Han, Y.; Sun, J.; Jiang, M.; Zu, G.; Song, X.; Zhu, W.; Ran, X. Improving the comprehensive mechanical property of the AlSi10Mg alloy via parameter adaptation of selective laser melting and heat treatment. *J. Alloys Compd.* **2024**, *981*, 173623. [[CrossRef](#)]
2. Kang, N.; El Mansori, M. A new insight on induced-tribological behaviour of hypereutectic Al-Si alloys manufactured by selective laser melting. *Tribol. Int.* **2020**, *149*, 105751. [[CrossRef](#)]
3. Goudar, D.M.; Raju, K.; Srivastava, V.C.; Rudrakshi, G.B. Effect of copper and iron on the wear properties of spray formed Al-28Si alloy. *Mater. Des.* **2013**, *51*, 383–390. [[CrossRef](#)]
4. Rao, J.H.; Zhang, Y.; Huang, A.; Wu, X.; Zhang, K. Improving fatigue performances of selective laser melted Al-7Si-0.6Mg alloy via defects control. *Int. J. Fatigue* **2019**, *129*, 105215. [[CrossRef](#)]
5. Martin, J.H.; Yahata, B.D.; Hundley, J.M.; Mayer, J.A.; Schaedler, T.A.; Pollock, T.M. 3D printing of high-strength aluminium alloys. *Nature* **2017**, *549*, 365–369. [[CrossRef](#)] [[PubMed](#)]
6. Mei, J.; Han, Y.; Zu, G.; Zhu, W.; Zhao, Y.; Chen, H.; Ran, X. Achieving Superior Strength and Ductility of AlSi10Mg Alloy Fabricated by Selective Laser Melting with Large Laser Power and High Scanning Speed. *Acta Metall. Sin. (Engl. Lett.)* **2022**, *35*, 1665–1672. [[CrossRef](#)]
7. Prashanth, K.G.; Scudino, S.; Klauss, H.J.; Surreddi, K.B.; Löber, L.; Wang, Z.; Chaubey, A.K.; Kühn, U.; Eckert, J. Microstructure and mechanical properties of Al-12Si produced by selective laser melting: Effect of heat treatment. *Mater. Sci. Eng. A* **2014**, *590*, 153–160. [[CrossRef](#)]
8. Park, T.-H.; Baek, M.-S.; Hyer, H.; Sohn, Y.; Lee, K.-A. Effect of direct aging on the microstructure and tensile properties of AlSi10Mg alloy manufactured by selective laser melting process. *Mater. Charact.* **2021**, *176*, 111113. [[CrossRef](#)]
9. Belov, N.A.; Eskin, D.G.; Avxentieva, N.N. Constituent phase diagrams of the Al-Cu-Fe-Mg-Ni-Si system and their application to the analysis of aluminium piston alloys. *Acta Mater.* **2005**, *53*, 4709–4722. [[CrossRef](#)]
10. Chuang, H.-C.; Lui, T.-S.; Chen, L.-H. Characteristics and Effects of Particle Morphology and Tensile Ductility Resulting from FSP of Al-Si-Cu-Ni Casting and Forging Piston. *Mater. Trans.* **2013**, *54*, 1373–1380. [[CrossRef](#)]
11. Rakhmonov, J.; Timelli, G.; Bonollo, F. Characterization of the solidification path and microstructure of secondary Al-7Si-3Cu-0.3Mg alloy with Zr, V and Ni additions. *Mater. Charact.* **2017**, *128*, 100–108. [[CrossRef](#)]
12. Manca, D.R.; Churyumov, A.Y.; Pozdniakov, A.V.; Ryabov, D.K.; Korolev, V.A.; Daubarayte, D.K. Novel heat-resistant Al-Si-Ni-Fe alloy manufactured by selective laser melting. *Mater. Lett.* **2019**, *236*, 676–679. [[CrossRef](#)]

13. Thapliyal, S.; Shukla, S.; Zhou, L.; Hyer, H.; Agrawal, P.; Agrawal, P.; Komarasamy, M.; Sohn, Y.; Mishra, R.S. Design of heterogeneous structured Al alloys with wide processing window for laser-powder bed fusion additive manufacturing. *Addit. Manuf.* **2021**, *42*, 102002. [[CrossRef](#)]
14. Zheng, Y.; Xiao, W.; Ge, S.; Zhao, W.; Hanada, S.; Ma, C. Effects of Cu content and Cu/Mg ratio on the microstructure and mechanical properties of Al–Si–Cu–Mg alloys. *J. Alloys Compd.* **2015**, *649*, 291–296. [[CrossRef](#)]
15. Rometsch, P.; Jia, Q.; Yang, K.; Wu, X. Aluminum alloys for selective laser melting—Towards improved performance. In *Additive Manufacturing for the Aerospace Industry*; Elsevier: Amsterdam, The Netherlands, 2019; pp. 301–325.
16. Medrano-Prieto, H.M.; Garay-Reyes, C.G.; Gómez-Esparza, C.D.; Estrada-Guel, I.; Aguilar-Santillan, J.; Maldonado-Orozco, M.C.; Martínez-Sánchez, R. Effect of Nickel addition and solution treatment time on microstructure and hardness of Al–Si–Cu aged alloys. *Mater. Charact.* **2016**, *120*, 168–174. [[CrossRef](#)]
17. Zhang, J.; Yan, P.; Yan, B. Effect of Different Heat Treatments on the Evolution of Novel Al–Si–Cu–Ni–Fe–Re Alloy Fabricated by Selective Laser Melting. *Metals* **2022**, *12*, 1827. [[CrossRef](#)]
18. Dai, H.; Song, Y.; Chen, H.; Miao, J. Directed Energy Deposition-Arc Repair Al6.5Cu2Ni0.3Ti0.5Zr0.25V Alloy: Microstructure Evolution and Strengthening Mechanism. *Adv. Eng. Mater.* **2024**, *26*, 2301772. [[CrossRef](#)]
19. Wang, H.; He, L.; Zhang, Q.; Yuan, Y. Influence of Ni Contents on Microstructure and Mechanical Performance of AlSi10Mg Alloy by Selective Laser Melting. *Materials* **2023**, *16*, 4679. [[CrossRef](#)] [[PubMed](#)]
20. Jandaghi, M.R.; Aversa, A.; Manfredi, D.; Calignano, F.; Lavagna, L.; Pavese, M. In situ alloying of AlSi10Mg-5 wt% Ni through laser powder bed fusion and subsequent heat treatment. *J. Alloys Compd.* **2022**, *904*, 164081. [[CrossRef](#)]
21. Ming, X.; Song, D.; Yu, A.; Tan, H.; Zhang, Q.; Zhang, Z.; Chen, J.; Lin, X. Effect of heat treatment on microstructure, mechanical and thermal properties of selective laser melted AlSi7Mg alloy. *J. Alloys Compd.* **2023**, *945*, 169278. [[CrossRef](#)]
22. Xue, Y.; Shao, Q.; Mu, J.; Ji, X.; Wang, X. Microstructure and compression performance of novel AlSi10Mg composite auxetic structures fabricated by additive manufacturing. *Mater. Sci. Eng. A* **2024**, *897*, 146330. [[CrossRef](#)]
23. Zhang, J.; Liu, Y.; Bayat, M.; Tan, Q.; Yin, Y.; Fan, Z.; Liu, S.; Hattel, J.H.; Dargusch, M.; Zhang, M.-X. Achieving high ductility in a selectively laser melted commercial pure-titanium via in-situ grain refinement. *Scr. Mater.* **2021**, *191*, 155–160. [[CrossRef](#)]
24. Wang, P.; Gammer, C.; Brenne, F.; Niendorf, T.; Eckert, J.; Scudino, S. A heat treatable TiB<sub>2</sub>/Al-3.5Cu-1.5Mg-1Si composite fabricated by selective laser melting: Microstructure, heat treatment and mechanical properties. *Compos. Part B Eng.* **2018**, *147*, 162–168. [[CrossRef](#)]
25. Thijs, L.; Kempen, K.; Kruth, J.-P.; Van Humbeeck, J. Fine-structured aluminium products with controllable texture by selective laser melting of pre-alloyed AlSi10Mg powder. *Acta Mater.* **2013**, *61*, 1809–1819. [[CrossRef](#)]
26. Wang, D.; Song, C.; Yang, Y.; Bai, Y. Investigation of crystal growth mechanism during selective laser melting and mechanical property characterization of 316L stainless steel parts. *Mater. Des.* **2016**, *100*, 291–299. [[CrossRef](#)]
27. Qian, B.; Saeidi, K.; Kvetková, L.; Lofaj, F.; Xiao, C.; Shen, Z. Defects-tolerant Co–Cr–Mo dental alloys prepared by selective laser melting. *Dent. Mater.* **2015**, *31*, 1435–1444. [[CrossRef](#)] [[PubMed](#)]
28. Chakraborty, N. The effects of turbulence on molten pool transport during melting and solidification processes in continuous conduction mode laser welding of copper–nickel dissimilar couple. *Appl. Therm. Eng.* **2009**, *29*, 3618–3631. [[CrossRef](#)]
29. Asta, M.; Beckermann, C.; Karma, A.; Kurz, W.; Napolitano, R.; Plapp, M.; Purdy, G.; Rappaz, M.; Trivedi, R. Solidification microstructures and solid-state parallels: Recent developments, future directions. *Acta Mater.* **2009**, *57*, 941–971. [[CrossRef](#)]
30. Prashanth, K.G.; Eckert, J. Formation of metastable cellular microstructures in selective laser melted alloys. *J. Alloys Compd.* **2017**, *707*, 27–34. [[CrossRef](#)]
31. Cahn, J.W. Free Energy of a Nonuniform System. II. Thermodynamic Basis. *J. Chem. Phys.* **1959**, *30*, 1121–1124. [[CrossRef](#)]
32. Division, C.; Ridge, O.; Sciences, P. Spinodal decomposition Fe–Cr alloys: Experimental study at the atomic level and comparison with computer models-development of morphology—I introduction and methodology. *Acta Metall. Mater.* **1995**, *43*, 3385–3401.
33. Caron, P.; Khan, T.; Veyssi re, P. On precipitate shearing by superlattice stacking faults in superalloys. *Philos. Mag. A* **1988**, *57*, 859–875. [[CrossRef](#)]
34. Cahn, J.W. On spinodal decomposition in cubic crystals. *Acta Metall.* **1962**, *10*, 179–183. [[CrossRef](#)]
35. Smith, D.W.; Elliott, C.M. Spinodal decomposition Fe–Cr alloys: Experimental study at the atomic level and comparison with computer models-development of morphology—III. Development of methodology. *Acta Metall. Mater.* **1995**, *43*, 3415–3426.
36. Tsai, M.-H.; Yeh, J.-W. High-Entropy Alloys: A Critical Review. *Mater. Res. Lett.* **2014**, *2*, 107–123. [[CrossRef](#)]
37. Li, N.; Li, Z.; Wei, Y. The Influence of Metastable Cellular Structure on Deformation Behavior in Laser Additively Manufactured 316L Stainless Steel. *Nanomaterials* **2021**, *11*, 2859. [[CrossRef](#)] [[PubMed](#)]
38. Wang, W.; Li, Q.; Du, A.; Fan, Y.; Zhao, X.; Yu, Y.; Ma, R.; Cao, X. Effects of Cu content on the wettability of SiC with Al–Ti–Si–xCu alloy and bending strength of resulting SiC matrix composite. *Ceram. Int.* **2018**, *44*, 5327–5335. [[CrossRef](#)]
39. Chen, G.; Yang, W.; Xin, L.; Wang, P.; Liu, S.; Qiao, J.; Hu, F.; Zhang, Q.; Wu, G. Mechanical properties of Al matrix composite reinforced with diamond particles with W coatings prepared by the magnetron sputtering method. *J. Alloys Compd.* **2018**, *735*, 777–786. [[CrossRef](#)]
40. Liu, Y.; Wang, R.; Peng, C.; Cai, Z.; Zhou, Z.; Li, X.; Cao, X. Microstructural evolution and mechanical performance of in-situ TiB<sub>2</sub>/AlSi10Mg composite manufactured by selective laser melting. *J. Alloys Compd.* **2021**, *853*, 157287. [[CrossRef](#)]
41. Yin, C.; Lu, Z.; Wei, X.; Yan, B.; Yan, P. High Bending Strength Hypereutectic Al-22Si-0.2Fe-0.1Cu-Re Alloy Fabricated by Selective Laser Melting. *Metals* **2021**, *11*, 528. [[CrossRef](#)]

42. Kekana, N.; Shongwe, M.B.; Mpofu, K.; Muvunzi, R. A review on factors influencing mechanical properties of AlSi12 alloy processed by selective laser melting. *Int. J. Adv. Manuf. Technol.* **2022**, *121*, 4313–4323. [[CrossRef](#)]
43. Prashanth, K.G.; Scudino, S.; Eckert, J. Defining the tensile properties of Al-12Si parts produced by selective laser melting. *Acta Mater.* **2017**, *126*, 25–35. [[CrossRef](#)]
44. Read, N.; Wang, W.; Essa, K.; Attallah, M.M. Selective laser melting of AlSi10Mg alloy: Process optimisation and mechanical properties development. *Mater. Des. (1980–2015)* **2015**, *65*, 417–424. [[CrossRef](#)]
45. Aksoy, S.; Kabakci, F.; Acarer, M.; Düzcükoğlu, H.; Ünüvar, E.; Fındık, F. Effect of Mg addition on microstructure and mechanical properties of AlSi12 alloy produced by high-pressure casting method. *Ind. Lubr. Tribol.* **2022**, *75*, 27–35. [[CrossRef](#)]
46. Zhao, Z.; Bai, P.; Misra, R.D.K.; Dong, M.; Guan, R.; Li, Y.; Zhang, J.; Tan, L.; Gao, J.; Ding, T.; et al. AlSi10Mg alloy nanocomposites reinforced with aluminum-coated graphene: Selective laser melting, interfacial microstructure and property analysis. *J. Alloys Compd.* **2019**, *792*, 203–214. [[CrossRef](#)]
47. Roth, C.C.; Tancogne-Dejean, T.; Mohr, D. Plasticity and fracture of cast and SLM AlSi10Mg: High-throughput testing and modeling. *Addit. Manuf.* **2021**, *43*, 101998. [[CrossRef](#)]
48. Li, W.; Li, S.; Liu, J.; Zhang, A.; Zhou, Y.; Wei, Q.; Yan, C.; Shi, Y. Effect of heat treatment on AlSi10Mg alloy fabricated by selective laser melting: Microstructure evolution, mechanical properties and fracture mechanism. *Mater. Sci. Eng. A* **2016**, *663*, 116–125. [[CrossRef](#)]
49. Hwang, W.J.; Bang, G.B.; Choa, S.-H. Effect of a Stress Relief Heat Treatment of AlSi7Mg and AlSi10Mg Alloys on Mechanical and Electrical Properties According to Silicon Precipitation. *Met. Mater. Int.* **2022**, *29*, 1311–1322. [[CrossRef](#)]
50. Croteau, J.R.; Griffiths, S.; Rossell, M.D.; Leinenbach, C.; Kenel, C.; Jansen, V.; Seidman, D.N.; Dunand, D.C.; Vo, N.Q. Microstructure and mechanical properties of Al-Mg-Zr alloys processed by selective laser melting. *Acta Mater.* **2018**, *153*, 35–44. [[CrossRef](#)]

**Disclaimer/Publisher’s Note:** The statements, opinions and data contained in all publications are solely those of the individual author(s) and contributor(s) and not of MDPI and/or the editor(s). MDPI and/or the editor(s) disclaim responsibility for any injury to people or property resulting from any ideas, methods, instructions or products referred to in the content.